Geophysical Journal International

Geophys. J. Int. (2024) **238,** 756–763
Advance Access publication 2024 April 18
GJI Seismology

https://doi.org/10.1093/gji/ggae145

A global SS precursor method for imaging discontinuities: the Moho and beyond

Yuhang Dai [1], Saikiran Tharimena [1,2], Catherine Rychert [1,3] and Nicholas Harmon [1,3]

[1] *School of Ocean and Earth Science, University of Southampton, Southampton SO14 3ZH, UK. E-mail: Y.Dai@soton.ac.uk*
[2] *Schibsted ASA, NO-0105, Oslo, Norway*
[3] *Geology and Geophysics, Woods Hole Oceanographic Institution, Woods Hole, MA 02543-1050, USA*

Accepted 2024 April 9. Received 2023 December 6; in original form 2023 February 27

SUMMARY

Imaging seismic velocity discontinuities within the Earth's interior offers important insight into our understanding of the tectonic plate, associated mantle dynamics, and the evolution of the planet. However, imaging velocity discontinuities in locations where station coverage is sparse, is sometimes challenging. Here we demonstrate the effectiveness of a new imaging approach using deconvolved *SS* precursor phases. We demonstrate its effectiveness by applying it to synthetic seismograms. We also apply it to ∼1.6 M *SS* precursor waveforms from the global seismic database (1990–2018) for comparison with CRUST1.0. We migrate to depth and stack the data in circular 6° bins. The synthetic tests demonstrate that we can recover Moho depths as shallow as 20 km. Globally, the Moho is resolved at 21–67 km depth beneath continental regions. The Moho increases in depth from 21 km ± 4 km beneath the continental shelf to 45–50 km beneath the continental interiors and is as deep as 67 ± 4 km beneath Tibet. We resolve the Moho in 77 percent of all continental bins, within 10 km of CRUST1.0, with all outliers located in coastal regions. We also demonstrate the feasibility of using this method to image discontinuities associated with the mantle transition zone with both synthetic and real data. Overall, the approach shows broad promise for imaging mantle discontinuities.

Key words: Body waves; Crustal imaging; Moho depth; Seismic discontinuities; Wave scattering and diffraction.

1 INTRODUCTION

Earth's radial structure is characterized by distinct boundaries associated with variations in seismic velocity and density (Dziewonski & Anderson 1981). Various physical and chemical processes are attributed to these variations. The shallowest of these boundaries include, for instance, the Moho, the lithosphere–asthenosphere boundary and the transition zone discontinuities. The Moho (Mohorovičić 1910) defines a boundary between the chemically distinct and seismically slow crust from the faster mantle beneath. The lithosphere–asthenosphere boundary represents the transition from a rheologically strong and seismically fast lithosphere, comprised of the crust and a section of the upper mantle, to the deeper, weaker and seismically slower asthenosphere (Eaton *et al.* 2009; Rychert & Shearer 2009; Fischer *et al.* 2010, 2020; Artemieva 2011; Rychert *et al.* 2018, 2020, 2021). The lithosphere is colder than the asthenosphere, and it may also be chemically distinct and/or partial melt may exist in the asthenosphere, further distinguishing the layers. The transition zone discontinuities are characterized by velocity increases with depth. They are typically interpreted as the pressure-induced solid-state transformation of olivine grains into denser crystal structures, or phase changes, predicted by laboratory experiments (Ringwood 1975): α olivine to β-spinel (wadslyite) at ∼410 km, β-spinel to ringwoodite at ∼520 km and ringwoodite to silicate perovskite and magnesiowüstite at ∼660 km (Ringwood 1975).

Imaging seismic velocity discontinuities globally can help us better understand the tectonic plate, mantle convection, and the evolution of the planet (Shearer 1991; Bostock 1999; Dai et al. 2023; Rychert *et al.* 2007; Rychert & Shearer 2011; Tharimena *et al.* 2017b); although, tight constraints on these discontinuities globally and self-consistently can be challenging. For example, both surface wave and body wave seismic tomography provide important constraints on the seismic velocity of the crust and the mantle (Montagner & Tanimoto 1991; Masters *et al.* 1996; Harmon *et al.* 2009; Ritsema *et al.* 2011), but the models have more difficulty resolving the exact location and character of sharp seismic discontinuities (Rychert *et al.* 2005, 2007). Receiver functions offer tighter constraints on the sharpness of velocity discontinuities but lack resolution in regions with sparse or no station coverage (Rychert *et al.* 2010). The highest resolution constraints come from active source studies, although these are limited in terms of spatial extent and the

depth to which they can image, with only very few studies imaging lithosphere–asthenosphere depths (Stern *et al.* 2015; Mehouachi & Singh 2018; Roy Chowdhury 2020).

SS phases are shear waves that have bounced once off the surface of the Earth roughly mid-way between the source and the receiver. *SS* precursors are underside reflections from discontinuities that arrive just before the main *SS* phases, which are sensitive to the region of their bounce point (Fig. 1a). These are referred to as *SdS*, where 'd' indicates the discontinuity of interest, for instance, *SmS* would refer to the *SS* reflection from the Moho. The advantage of these phases is that they offer resolution in locations where station coverage is sparse. However, *SS* waveforms and their precursors are relatively long-period waveforms. Precursors reflected from shallow discontinuities like the Moho and the lithosphere–asthenosphere boundary typically interfere with the surface-reflected *SS* waveforms, making them difficult to distinguish. Therefore, *SS* precursors have mostly been used to image deeper discontinuities such as the transition zone discontinuities (Flanagan & Shearer 1998; Houser *et al.* 2008; Huang *et al.* 2019; Frazer & Park 2023). To minimize waveform interference Schmerr (2012) considered acceleration seismograms, which are effectively filtered to higher frequencies and carefully selected data. The waveforms were stacked in bins and a discontinuity was detected approximately at lithosphere–asthenosphere depths (40–75 km) intermittently across the Pacific. In another approach Heit *et al.* (2010) deconvolved the *SS* waveform from itself before migrating and stacking in bins, imaging a discontinuity related to the Moho and the lithosphere–asthenosphere boundary beneath Asia. Rychert & Shearer (2010) developed a strategy to image discontinuities using *SS*-precursors by performing waveform modelling on the sidelobes of the stacked *SS* waveforms. Synthetic waveforms were calculated by convolving a reference *SS* stack with impulse operators corresponding to a variety of discontinuity depths and characters, and the best-fitting discontinuity was determined via a grid search approach. They validated the method at shallow Moho depths by demonstrating agreement with the CRUST2.0 (Bassin *et al.* 2000) and Mixture Density Network (MDN; Meier *et al.* 2007) models in bins across Asia and extended the method to image the lithosphere–asthenosphere boundary across the Pacific using an attenuated *S* wave as the reference waveform (Rychert & Shearer 2010, 2011). There was general agreement between the lithosphere-asthenosphere boundary depths from the work of Schmerr et al., (2012) and the work of Rychert & Shearer (2011) as described in the work of Rychert et al., 2012. Tharimena *et al.* (2017b) followed a similar procedure as Rychert & Shearer (2011) to image lithosphere–asthenosphere structure beneath the Pacific but implemented a differential evolution algorithm (Storn & Price 1997; Price *et al.* 2005) to minimize both the model storage size and computation time in comparison to a typical grid search. The inclusion of 7 additional years of data (1990–2014 instead of 1990–2007) yielded a threefold increase in the number of waveforms and a higher resolution result in which greater numbers of parameters could be explored. The study found discontinuities consistent with Schmerr (2012) and Rychert & Shearer (2011) but also found evidence for locations where either two discontinuities exist in depth and/or lithosphere–asthenosphere boundary depths vary laterally within a Fresnel zone of the waveforms.

Here we develop an approach to clearly image seismic discontinuities via deconvolution. We also incorporate an additional 4 years of data in comparison to Tharimena *et al.* (2017b). We focus on the *SS* precursor phases that reflect at the Moho (*SmS*) for validation purposes. We demonstrate the validity of our approach by applying it to synthetic seismograms. We also validate our approach by comparing the recovered global Moho depths with those from the CRUST1.0 model (Laske *et al.* 2012). Finally, we discuss the potential of this method for imaging other discontinuities.

2 METHODS

2.1 *SS* data

We use the Incorporated Research Institutions for Seismology (IRIS) broad-band data set from 1990 to 2018, with event-to-station (epicentral) distances of 85°–150°, for events with $M_w > 5.5$. Previous work has used a slightly more restricted range, for example 90°–140° (Rychert & Shearer 2010). However, this choice does not appear to strongly contaminate our resolution, as we will describe in the results and discussion section. We restricted our analysis to raw data from broadband channels (1–8 samples per second), and events with source depths <75 km to minimize complications from depth phases. The seismic records are corrected to remove instrument responses and then rotated to radial and transverse components. We consider only the transverse components.

We convert all seismograms from displacement to acceleration, and then Hilbert transform them to produce symmetric *SS* pulses (Oppenheim & Schafer 1975; Rychert & Shearer 2010). The waveforms are resampled to 10 samples per second and bandpass filtered with corners at 0.02 and 0.5 Hz. However, given the frequency content and dominant period of *SS* waves (∼15 s), there is not much frequency content above this in the waveforms (Rychert & Shearer 2011). An automated procedure is used to eliminate incomplete seismic records. We also use an automated procedure to centre the waveforms on the *SS* phase, which is picked as the maximum positive or negative amplitude in a 10-s time window before and after the theoretical *SS* arrival time. The amplitude of the centred waveform is normalized to unit amplitude. We compute the signal-to-noise ratio (SNR) for each record as the ratio of the maximum amplitude of the seismic phase to the standard deviation in a time window 270 s to 30 s preceding the *SS* pulse. Visual inspection of a random sample of 2000 waveforms shows that the waveforms are generally poor quality for SNR < 3. Therefore, waveforms with SNR < 3 are rejected. In addition, seismic records with amplitude >1 within a 90 s window preceding the normalized *SS* pulse are rejected. Finally, records with long-period noise evaluated as those with zero-crossings that occur at > 20 s intervals are also rejected. We obtain 4 962579 seismic records that fit the source parameters described above, 1648704 of which also fit the signal-to-noise criteria. Our data provides improved spatial coverage over previous studies (Fig. 2).

2.2 Binning schemes

Here we define a global binning scheme (Fig. 2) for stacking waveforms. We divide the surface of the Earth into evenly distributed 6° circular bins with 30 percent overlap, resulting in 1146 bins.

SS precursors have saddle-shaped Fresnel zones (Tharimena *et al.* 2016). However, this effect can be mitigated by stacking waveforms along different azimuths, which results in a more circular region of sensitivity centred on our bins and the sensitivity region of the precursors (Fig. 1b). The large number of waveforms (>1000) and better azimuthal coverage in each bin compared to our previous work, minimizes the effect of off-axis structures in our study. In addition, we also linearly weight the waveforms depending on their

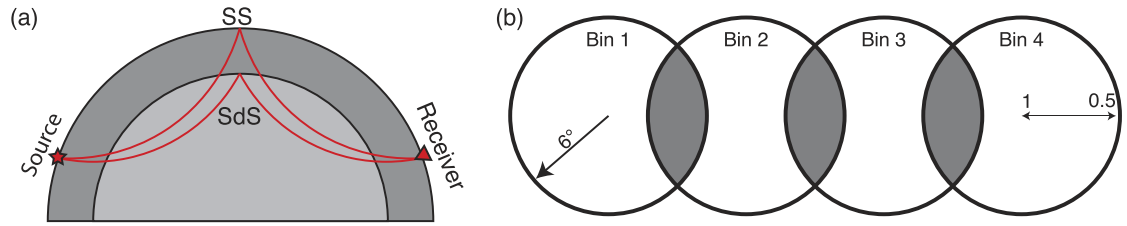

Figure 1. Ray paths and binning. (a) Schematic showing ray paths of the *SS* and the *SdS* phases, which are sensitive to the structure beneath the bounce point, roughly halfway between the source and the receiver. *SdS* refers to the underside reflection of the *S* wave at a discontinuity, located at 'd' km depth, for example the Moho, 410 and 660. (b) Schematic representation of binning and weighting. The shaded area shows the region of overlap between bins. The 1 and 0.5 labels indicate the weighting that is applied to the data, which varies linearly from 1 at the centre of the bin to 0.5 at the edge of the bin.

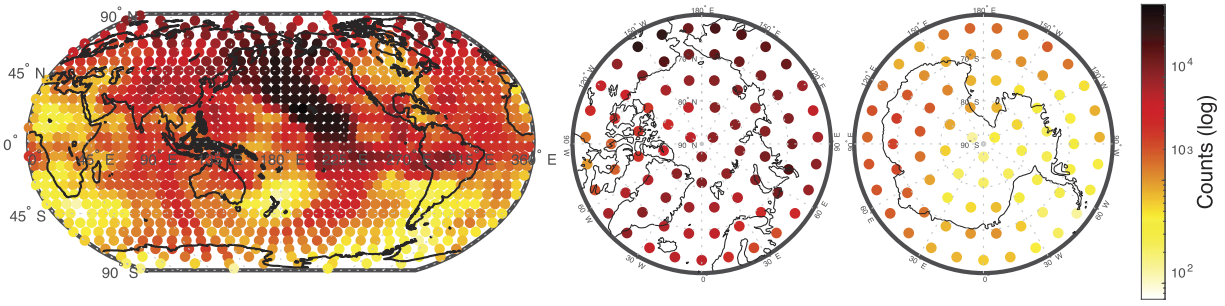

Figure 2. Hits per bouncepoint bin. Maps showing the number of waveforms with *SS* phases and precursors in each bin that satisfy our requirements. Most of the Earth is shown (left) with the northern (central) and southern (right) hemisphere projections shown. Maps include hits corresponding to the 1648704 *SS* waveforms that satisfy our selection criteria.

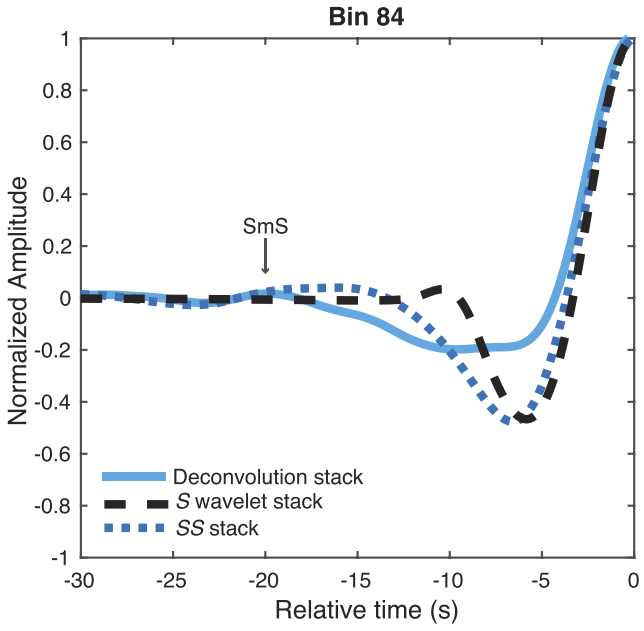

Figure 3. Waveform examples from bin 84, located in North America. The stack of all SS waveforms (blue dashed), an example of an S source stack that was used to deconvolve the 30corresponding individual SS waveforms in bin 84 (black dashed), and the stack of deconvolved SS waveforms (blue) are shown. The example S stack corresponds to an earthquake of Mw = 6.9 that occurred at 06:48:10 on 19 February, 1990, west of Luganville, Vanuatu. The *SmS* phase is indicated by an arrow.

distance from the bin centre. We assign the highest weight of 1 to waveforms with bounce points closest to the bin centre and a weight of 0.5 to waveforms with bounce points on the edges of the circular bin. This further ensures that the *SS* precursor stacks are more sensitive to the structure beneath the bounce points.

2.3 S data and processing source wavelets

The *SS* phases are Hilbert transformed relative to the *S* phases (Choy & Richards 1975). Therefore, the deconvolution of stacked source *S* phases from Hilbert transformed *SS* phases has the potential to separate the *SS* and *SdS* responses (Fig. 3). We create event *S*-wave source stacks for each event that will be deconvolved from the corresponding individual *SS* waveforms (Rychert & Shearer 2011; Tharimena *et al.* 2016; Tharimena *et al.* 2017a,b). We follow similar processing steps described above for the *SS*. We use seismic records from 1990 to 2018, with epicentral distances of 25°–80°, for events with magnitudes $M_w > 5.5$, and source depths <75 km. We resample the data to 10 Hz and then apply a band-pass filter with corners at 0.02 and 0.5 Hz. We use an automated approach to pick the seismic *S* phase as the maximum positive or negative amplitude pulse in a 10-s window before and after the theoretical *S* arrival time. The signal-to-noise ratio for each seismic record is calculated by comparing the maximum absolute value to the standard deviation in a time window 100 s–20 s before the *S* phase. Waveforms with SNR < 2.8 are generally found to be of poor quality, with seismic coda before the S phase containing amplitudes as large as or greater than the *S* phase, and therefore they are rejected. The seismic records are then cut to a 40 s window centred on the picked *S* phase. The

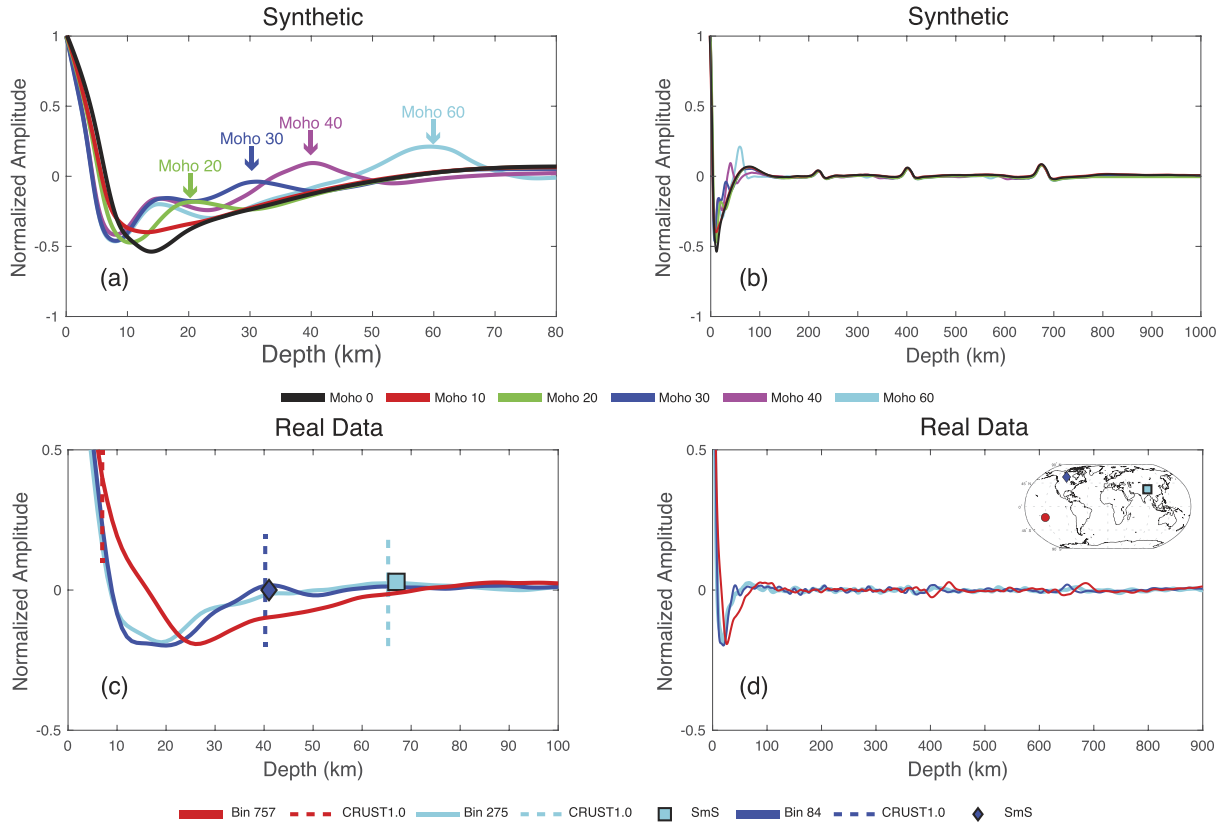

Figure 4. Synthetic and real examples. (a) *SS* synthetics were calculated for models modified from PREM to incorporate a Moho at 10, 20, 30, 40,and 60 km depth and a model without a Moho. The synthetics were processed in the same way we process the data. We calculated waveforms from a range of epicentral distances (each degree from 85° to 150°) and stacked the resulting waveforms on the *SS* phase and migrated to depth. The resolved corresponding Moho depths are marked by arrows. (b) Same as (a) but in a longer depth window. (c) Examples of real data in Bin 84, 757 and 275. Bin 757 represents an oceanic region where we failed to resolve the Moho. Bin 84 represents normal crust in North America , and bin 275 represents a bin with thick crust in Tibet, which we resolve (diamond and square) in comparison to CRUST1.0 (dashed line). (d) Same as (c) but in a longer depth window. Markers in the inset map show the locations of these three bins, blue diamond for Bin 84, cyan square for Bin 275 and red circle for Bin 757.

records are normalized to unit amplitude, and a 5 s cosine taper is applied to the ends of the wavelet. Finally, the source wavelets from all global receivers for a particular seismic event are stacked, scaling by individual SNRs to produce source stacks. We obtain 11484 unique source stacks, for the events from 1990 to 2018 in our study.

2.4 Deconvolution, migration and stacking *SS* waveforms

We deconvolve the *S* wavelet stack of the corresponding event from each *SS* waveform using an extended time multitaper frequency domain deconvolution method (Helffrich 2006; Rychert *et al.* 2012; Fig. 3). The deconvolution method is a hybrid between multitaper deconvolution and Welch's method for spectra estimation. Specifically, the method sums multitaper cross and auto spectral estimates on several overlapping windows across the records and then performs the deconvolution. We use a 30 s window, with a 50 percent overlap on each window, a time-bandwidth product of 3 that translates to a frequency bandwidth of permissible spectral leakage of 0.2 Hz and 4 tapers (Shibutani *et al.* 2008). This results in an impulse response function that corresponds to the discontinuity structure beneath the bounce point. Deconvolutions of individual waveforms are normalized to the *SS* phase amplitude. The normalized impulse response functions with amplitudes larger than 1 in precursor sections are rejected.

The impulse response functions are then migrated to depth, stacked, and Moho depths are estimated. For the crust, we use a smoothed version of CRUST1.0, corresponding to the average thickness and velocity within the 6° bin. For the mantle we use the IASP91 model, beginning at subcrustal depths. Finally, we stack the migrated impulse response functions scaled according to their signal-to-noise ratio and distance from the bin centre (Section 2.2). We then search automatically for the peak in the stack arriving before the main *SS* pulse, which is likely related to the Moho discontinuity.

2.5 Validation

We validate our approach by applying it to synthetic seismogram data calculated using the spectral element solver AxiSEM (Nissen-Meyer *et al.* 2014) which creates full waveform synthetics assuming a spherically symmetric earth model. AxiSEM separates the problem of wave propagation in a symmetric medium into an analytical solution of the problem in the azimuthal (ϕ) direction perpendicular to the source–receiver plane and a numerical spectral-element discretization within the in-plane r, θ, which reduces the numerical cost to that of about a 2-D method (Nissen-Meyer *et al.* 2007) and includes attenuation and anisotropy. We used a source with the following focal mechanism parameters: $M_0 = 1e^{21}$, strike = 32, dip = 62. We then generate wavefields for the 1-D velocity models

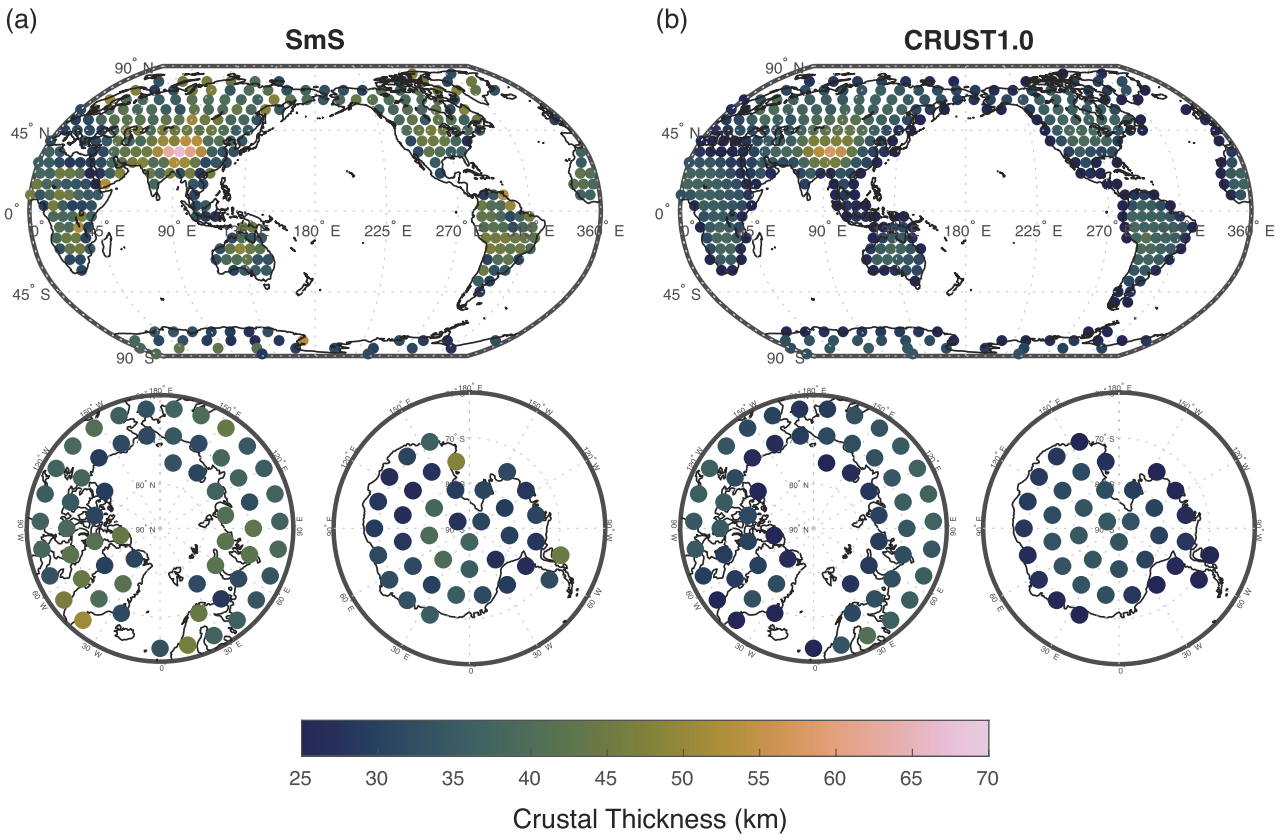

Figure 5. Crustal thickness. (a) Crustal thickness measured from *SmS* phases. Top panels: global view; Bottom left-hand panel: Antarctic view; Bottom right-hand panel: Arctic view. (b) Same as (a) but for crustal thickness from CRUST1.0 model.

modified from the reference earth model PREM (Dziewonski & Anderson 1981) including a velocity increase at a range of potential Moho depths: 10, 20, 30, 40 and 60 km and one without crust. For models with Moho depths at 10 and 20 km, we replace the upper crustal layer ($\leq$15 km) in the PREM model with lower crust parameters and set the Moho at corresponding depths. For other models with deeper Mohos we extend the deeper crustal layer to the corresponding Moho depths. We process the synthetics in the same way we process the data and use the input model to translate the resulting impulse response functions to depth.

*Instaseis (*van Driel *et al.* 2015*)*, a Python package, is used to reconstruct seismograms for a source defined by moment-tensor and receiver locations using the pre-calculated wavefield databases. This is possible due to the reciprocity of the Green's function which permits switching the location of source and receiver of a seismic wavefield. *Instaseis* uses the stored displacement wavefield to calculate strain, which enables the simulation of arbitrary moment tensors and source time functions.

We also compare the depth of the *SmS* phase in each data bin to CRUST1.0. The standard deviation of error between resolved crustal thickness and CRUST1.0 is 4 km, which is the value we report as the error here.

3 RESULTS AND DISCUSSION

The resolution testing with synthetics shows that we can resolve discontinuities as shallow as 20 km depth (Fig. 4). We also resolve phases at 15 km depth for the synthetic models with Mohos at $\geq$30 km, since this internal crustal discontinuity exists in the PREM model (Fig. 4a). However, it does not impact the resolution of the deeper Moho depths.

For real data, regions with Moho depths <20 km are not well-resolved. Therefore, we focus only on discontinuities at $\geq$20 km depth. This includes 397 bins out of 415 bins with continental crust according to the 3SMAC (Nataf & Ricard 1996) classification.

Our *SS* precursor method applied to the data resolves the Moho globally beneath the continents well. We image a Moho at 21–67 km depth beneath the continents. The thickest crust, 67 $\pm$ 4 km depth, is imaged beneath the Himalayan region of Asia.

Our results are in excellent agreement with crustal thickness from CRUST1.0 averaged over our bins in continental regions (Laske *et al.* 2012) (Fig. 5). Our result is a minimum of 9 km shallower than CRUST1.0 in all well-resolved locations (Fig. 6). Our result is over 10 km deeper than CRUST1.0 in 19 percent of bins with crust >20 km based on depths from CRUST1.0. The outliers are all located in coastal areas except for 1 bin in Africa. The reason for this asymmetry and the fact that *SS* cannot resolve the coastal bins is that the depths of the CRUST1.0 model averaged over the bin areas are relatively shallow, given the nearby oceanic crust. However, shallow, oceanic Moho phases fall within the main *SS* pulse and do not affect its sidelobe or resulting Moho depth (Rychert & Shearer 2010). Therefore, the only resolved *SS* Moho in these coastal regions is from the thicker continental regions. In addition, thick sediments near coastal regions could add greater complexity (Wang *et al.* 2022). Excluding the 76 outlier coastal bins, observed crustal thicknesses of the remaining 321 bins are correlated with the CRUST1.0 model at 0.81, and 70 percent of those bins are resolved within 5 km of CRUST1.0, with a correlation coefficient of 0.93.

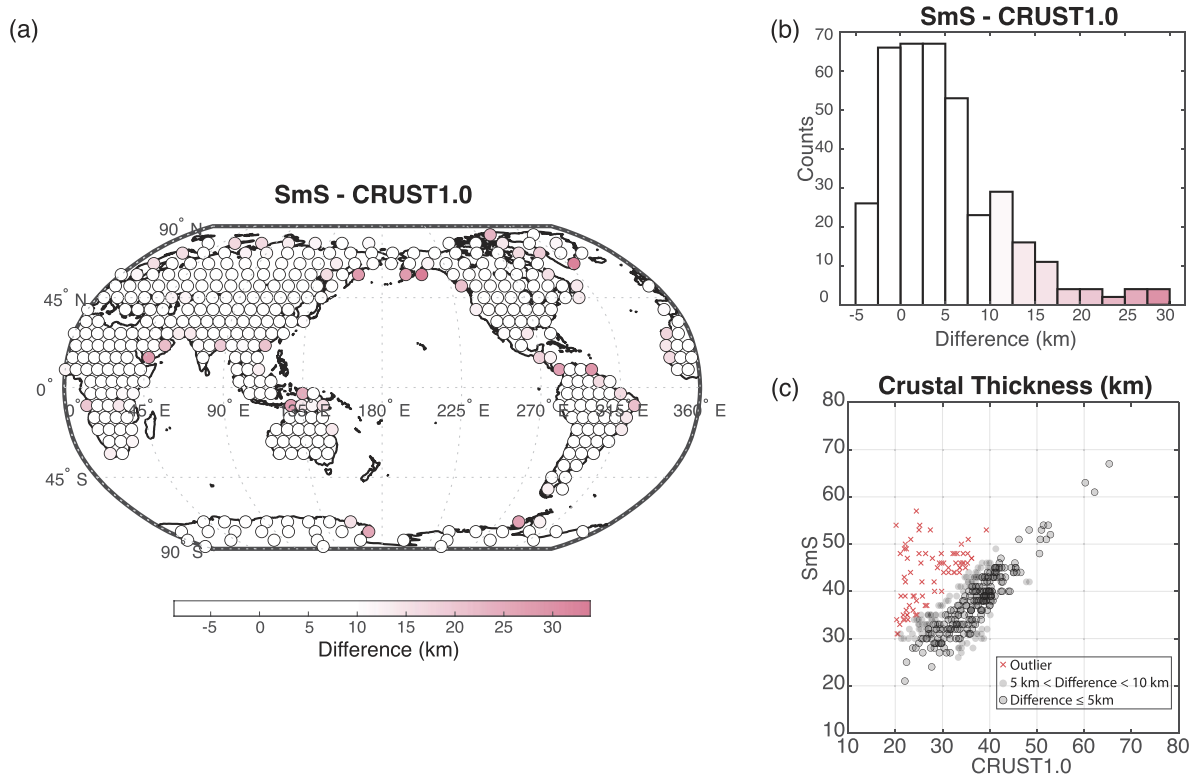

Figure 6. Comparisons to CRUST1.0. (a) Differences between crustal thickness from *SS* precursor, *SmS* phases, and the CRUST1.0 model. (b) Histogram of the differences in crustal thicknesses between *SmS* and the CRUST1.0 model. (c) Comparisons of crustal thickness from *SmS* phases, and the CRUST1.0 model. Semi-transparent dots show cases with differences of 5–10 km from CRUST1.0. Semi-transparent dots with outlines show cases with differences of ≤5 km from CRUST1.0. Red crosses show data with differences larger than 10 km, shown as pink dots in (a), which are primarily in coastal regions.

This verifies that this method can be used to resolve discontinuities, although we do not believe that it supersedes CRUST1.0.

Overall, the increase in data quantity and improved method demonstrate enhanced resolution capabilities in comparison to previous work (Rychert & Shearer 2010). Rychert & Shearer (2010) resolved the Moho in 30 10° bins beneath Asia and at depths >25 km, a region of particularly large bounce point coverage and deep Moho depths, and found Moho depths correlated with CRUST2.0 at 0.82. However, we resolve the Moho beneath 321 bins in continental regions at depths as shallow as 20 km. This method will be useful for constraining the depths of other deeper discontinuities such as he LAB or those of the mantle transition zone. From synthetic testing, despite variations in crustal thickness, the discontinuities at 200, 400 and 670 km in the PREM models were well resolved. Moreover, we also find clear phases associated with the mantle transition zone in real data even though the parameters, for example epicentre distances, and bandpass, used in this work may not be ideal to image them (Fig. 4).

4 CONCLUSION

We developed a new *SS* precursor imaging method that achieves high-resolution imaging, 6° × 6°, of discontinuities as shallow as 20 km depth. We verified that the method resolves structures as shallow as 20 km depth by applying it to AxiSEM synthetics calculated for a PREM model modified to include velocity increases at potential Moho depths between 10 and 60 km depth. We also validated the method by comparing the Moho resolved by data stacked in 6° bins to CRUST1.0. We find that we can resolve Moho depths in 77 percent of all continental bins, within 10 km of CRUST1.0, with all outliers located in coastal regions. Both synthetic and data examples demonstrate mantle transition zone discontinuities are also well resolved. Overall, this approach shows much promise for imaging discontinuity structure of other discontinuities at high resolution in the future.

ACKNOWLEDGMENTS

This work is supported in part by Natural Environment Research Council, UK grant NE/M003507/1 (PI-LAB), the European Research Council (GA 638665) (EURO-LAB), and the National Science Foundation grants NSF-EAR-2333101 and NSF-EAR-2147918. The authors acknowledge the use of the IRIDIS High Performance Computing Facility, and associated support services at the University of Southampton in the completion of this work.

AUTHOR CONTRIBUTIONS

Yuhang Dai (Formal analysis [equal], Investigation [equal], Methodology [lead], Software [lead], Validation [equal], Visualization [equal], Writing – review & editing [equal]), Saikiran Tharimena (Conceptualization [equal], Data curation [lead], Formal analysis [equal], Investigation [equal], Methodology [equal], Visualization [equal], Writing – original draft [equal]), Catherine Rychert (Conceptualization [equal], Formal analysis [equal], Funding acquisition [lead], Investigation [equal], Methodology [equal], Resources [equal], Supervision [equal], Visualization [supporting], Writing – original draft [equal]) and Nicholas Harmon (Conceptualization

[equal], Data curation [supporting], Formal analysis [equal], Funding acquisition [equal], Investigation [equal], Methodology [equal], Resources [equal], Supervision [equal], Visualization [supporting], Writing – original draft [equal]).

DATA AND CODE AVAILABILITY

Global data used for this study is available from the Incorporated Research Institutions for Seismology (IRIS) Data Management Center (DMC) website https://ds.iris.edu/ds/nodes/dmc. AxiSEM/Instaseis database of PREM is available at IRIS DMC. A version of the code used in this work is available upon request.

REFERENCES

Artemieva, I., 2011. *The Lithosphere: An Interdisciplinary Approach,* Cambridge Univ. Press. doi: 10.1017/CBO9780511975417.

Bassin, C., Laske, G. & Masters, G., 2000. The current limits of resolution for surface wave tomography in North America, *EOS, Trans. Am. geophys. Un.,* **81,** F897.

Bostock, M.G., 1999. Seismic imaging of lithospheric discontinuities and continental evolution, *Lithos,* **48**(1-4), 1–16.

Choy, G.L. & Richards, P.G., 1975. Pulse distortion and hilbert transformation in multiply reflected and refracted body waves, *Bull. seism. Soc. Am.,* **65**(1), 55–70.

Dai, Y., Rychert, C. A. & Harmon, N.. 2023 Seismic Imaging Beneath Cascadia Shows Shallow Mantle Flow Patterns Guide Lower Mantle Upwellings. *Journal of Geophysical Research: Solid Earth* **128**(9), e2023JB026374. doi: 10.1029/2023JB026374.

Dziewonski, A.M. & Anderson, D.L., 1981. Preliminary Reference Earth Model, *Phys. Earth planet. Inter.,* **25**(4), 297–356.

Eaton, D.W., Darbyshire, F., Evans, R.L., Grutter, H., Jones, A.G. & Yuan, X.H., 2009. The elusive lithosphere-asthenosphere boundary (LAB) beneath cratons, *Lithos,* **109**(1-2), 1–22.

Fischer, K. M., Rychert, C. A., Dalton, C. A., Miller, M. S., Beghein, C. & Schutt, D.L. 2020 A comparison of oceanic and continental mantle lithosphere. *Physics of the Earth and Planetary Interiors* **309**: 106600. https://doi.org/10.1016/j.pepi.2020.106600

Fischer, K.M., Ford, H.A., Abt, D.L. & Rychert, C.A., 2010. The lithosphere-asthenosphere boundary, *Annu. Rev. Earth planet. Sci.,* **38**(1), 551–575.

Flanagan, M.P. & Shearer, P.M., 1998. Global mapping of topography on transition zone velocity discontinuities by stacking SS precursors, *J. geophys. Res.,* **103**(B2), 2673–2692.

Frazer, W.D. & Park, J., 2023. High-resolution mid-mantle imaging with multiple-taper SS-precursor estimates, *Geophys. J. Int.,* **233**(2), 1356–1371.

Harmon, N., Forsyth, D.W. & Weeraratne, D.S., 2009. Thickening of young Pacific lithosphere from high-resolution Rayleigh wave tomography: a test of the conductive cooling model, *Earth planet. Sci. Lett.,* **278**(1-2), 96–106.

Heit, B., Yuan, X.H., Bianchi, M., Kind, R. & Gossler, J., 2010. Study of the lithospheric and upper-mantle discontinuities beneath eastern Asia by SS precursors, *Geophys. J. Int.,* **183**(1), 252–266.

Helffrich, G., 2006. Extended-time multitaper frequency domain cross-correlation receiver-function estimation, *Bull. seism. Soc. Am.,* **96**(1), 344–347.

Houser, C., Masters, G., Flanagan, M. & Shearer, P., 2008. Determination and analysis of long-wavelength transition zone structure using SS precursors, *Geophys. J. Int.,* **174**(1), 178–194.

Huang, Q., Schmerr, N., Waszek, L. & Beghein, C., 2019. Constraints on seismic anisotropy in the mantle transition zone from long-period SS precursors, *J. geophys. Res.,* **124**(7), 6779–6800.

Laske, G., Masters, G., Ma, Z. & Pasyanos, M., 2012. CRUST1.0: an updated global model of Earth's crust, *Geophys. Res. Abstr.,* **14,** http://igppweb.ucsd.edu/~gabi/crust1.html.

Masters, G., Johnson, S., Laske, G. & Bolton, H., 1996. A shear-velocity model of the mantle, *Phil. Trans. R. Soc.,* **354**(1711), 1385–1410.

Mehouachi, F. & Singh, S.C., 2018. Water-rich sublithospheric melt channel in the equatorial Atlantic Ocean, *Nat. Geosci.,* **11**(1), 65–69.

Meier, U., Curtis, A. & Trampert, J., 2007. Global crustal thickness from neural network inversion of surface wave data, *Geophys. J. Int.,* **169**(2), 706–722.

Mohorovičić, A., 1910. Potres od 8. X. 1909. Godišnje Izvješće Zagrebačkog Meteorološkog Opservatorija za godinu 1909.

Montagner, J.P. & Tanimoto, T., 1991. Global upper mantle tomography of seismic velocities and anisotropies, *J. geophys. Res.,* **96,** 15.

Nataf, H.C. & Ricard, Y., 1996. 3SMAC: an a priori tomographic model of the upper mantle based on geophysical modeling, *Phys. Earth planet. Inter.,* **95**(1-2), 101–122.

Nissen-Meyer, T., Fournier, A. & Dahlen, F.A., 2007. A two-dimensional spectral-element method for computing spherical-earth seismograms—I. Moment-tensor source, *Geophys. J. Int.,* **168**(3), 1067–1092.

Nissen-Meyer, T., van Driel, M., Stähler, S.C., Hosseini, K., Hempel, S., Auer, L., Colombi, A. & Fournier, A., 2014. AxiSEM: broadband 3-D seismic wavefields in axisymmetric media, *Solid Earth,* **5**(1), 425–445.

Oppenheim, A.V. & Schafer, R.W., 1975. *Digital Signal Processing,* Prentice-Hall, Inc.

Price, K.V., Storn, R.M. & Lampinen, J.A., 2005. *Differential Evolution: a Practical Approach to Global Optimization,* Springer.

Ringwood, A.E., 1975. *Composition and Petrology of the Earth's Mantle,* McGraw-Hill.

Ritsema, J., Deuss, A., van Heijst, H.J. & Woodhouse, J.H., 2011. S40RTS: a degree-40 shear-velocity model for the mantle from new Rayleigh wave dispersion, teleseismic traveltime and normal-mode splitting function measurements, *Geophys. J. Int.,* **184**(3), 1223–1236.

Roy Chowdhury, K., 2020. Deep seismic reflection and refraction profiling, in *Encyclopedia of Solid Earth Geophysics,* pp. 1–18, ed. Gupta, H.K., Springer International Publishing. doi:10.1007/springerreference_225584.

Rychert, C. A., Tharimena, S., Harmon, N., Wang, S., Constable, S., Kendall, J. M., Bogiatzis, P., Agius, M. R. & Schlaphorst, D. 2021 A dynamic lithosphere-asthenosphere boundary near the equatorial Mid-Atlantic Ridge. *Earth and Planetary Science Letters* **566**: 116949. doi: 10.1016/j.epsl.2021.116949.

Rychert, C.A. & Shearer, P.M., 2009. A global view of the lithosphere-asthenosphere boundary, *Science,* **324**(5926), 495–498.

Rychert, C.A. & Shearer, P.M., 2010. Resolving crustal thickness using SS waveform stacks, *Geophys. J. Int.,* **180**(3), 1128–1137.

Rychert, C.A. & Shearer, P.M., 2011. Imaging the lithosphere-asthenosphere boundary beneath the Pacific using SS waveform modeling, *J. geophys. Res.,* **116**(B7), doi:10.1029/2010JB008070.

Rychert, C.A., Fischer, K.M. & Rondenay, S., 2005. A sharp lithosphere-asthenosphere boundary imaged beneath eastern North America, *Nature,* **436**(7050), 542–545.

Rychert, C.A., Harmon, N. & Tharimena, S., 2018. Seismic imaging of the base of the ocean plates, in *Lithospheric Discontinuities,* pp. 71–87, eds Yuan, H. & Romanowicz, B., Geophysical Monograph Series, AGU.

Rychert, C.A., Harmon, N., Constable, S. & Wang, S., 2020. The nature of the lithosphere-asthenosphere boundary, *J. geophys. Res.,* **125**(10), e2018JB016463.

Rychert, C.A., Rondenay, S. & Fischer, K.M., 2007. P-to-S and S-to-P imaging of a sharp lithosphere-asthenosphere boundary beneath eastern North America, *J. geophys. Res.,* **112**(B8), doi:10.1029/2006jb004619.

Rychert, C.A., Schmerr, N. & Harmon, N., 2012. The Pacific lithosphere-asthenosphere boundary: seismic imaging and anisotropic constraints from SS waveforms, *Geochem. Geophys. Geosyst.,* **13,** Q0AK10. doi:10.1029/2012gc004194.

Rychert, C.A., Shearer, P.M. & Fischer, K.M., 2010. Scattered wave imaging of the lithosphere–asthenosphere boundary, *Lithos,* **120**(1-2), 173–185.

Schmerr, N., 2012. The Gutenberg discontinuity: melt at the lithosphere-asthenosphere boundary, *Science,* **335**(6075), 1480–1483.

Shearer, P.M., 1991. Constraints on upper mantle discontinuities from observations of long-period reflected and converted phases, *J. geophys. Res.,* **96**(B11), 18 147–18 182.

Shibutani, T., Ueno, T. & Hirahara, K., 2008. Improvement in the extended-time multitaper receiver function estimation technique, *Bull. seism. Soc. Am.,* **98**(2), 812–816.

Stern, T.A. *et al.* 2015. A seismic reflection image for the base of a tectonic plate, *Nature,* **518**(7537), 85–88.

Storn, R. & Price, K., 1997. Differential evolution—a simple and efficient heuristic for global optimization over continuous spaces, *J. Global Optim.,* **11**(4), 341–359.

Tharimena, S., Rychert, C. & Harmon, N., 2017a. A unified continental thickness from seismology and diamonds suggests a melt-defined plate,. *Science,* **357**(6351), 580–583.

Tharimena, S., Rychert, C., Harmon, N. & White, P., 2017b. Imaging Pacific lithosphere seismic discontinuities—insights from SS precursor modeling, *J. Geophys. Res.,* **122**(3), 2131–2152.

Tharimena, S., Rychert, C.A. & Harmon, N., 2016. Seismic imaging of a mid-lithospheric discontinuity beneath Ontong Java Plateau, *Earth planet. Sci. Lett.,* **450,** 62–70. doi: 10.1016/j.epsl.2016.06.026.

van Driel, M., Krischer, L., Stähler, S.C., Hosseini, K. & Nissen-Meyer, T., 2015. Instaseis: instant global seismograms based on a broadband waveform database, *Solid Earth,* **6**(2), 701–717.

Wang, P., Zhou, Y., Xu, M., Zhang, H., Chen, X. & Guo, L., 2022. Investigation of effects of near-surface complexities on measurement of mantle discontinuity using SS and its precursors, *J. geophys. Res.,* **127**(9), e2022JB024485.